Polarization Topology at the Nominally Charged Domain Walls in Uniaxial Ferroelectrics

Yurii Tikhonov, Jesi R. Maguire, Conor J. McCluskey, James P. V. McConville, Amit Kumar, Haidong Lu, Dennis Meier, Anna Razumnaya, John Martin Gregg, Alexei Gruverman, Valerii M. Vinokur,* and Igor Luk'yanchuk

Ferroelectric domain walls provide a fertile environment for novel materials physics. If a polarization discontinuity arises, it can drive a redistribution of electronic carriers and changes in band structure, which often result in emergent 2D conductivity. If such a discontinuity is not tolerated, then its amelioration usually involves the formation of complex topological patterns, such as flux-closure domains, dipolar vortices, skyrmions, merons, or Hopfions. The degrees of freedom required for the development of such patterns, in which dipolar rotation is a hallmark, are readily found in multiaxial ferroelectrics. In uniaxial ferroelectrics, where only two opposite polar orientations are possible, it has been assumed that discontinuities are unavoidable when antiparallel components of polarization meet. This perception has been borne out by the appearance of charged conducting domain walls in systems such as hexagonal manganites and lithium niobate. Here, experimental and theoretical investigations on lead germanate ($Pb_5Ge_3O_{11}$) reveal that polar discontinuities can be obviated at head-to-head and tail-to-tail domain walls by mutual domain bifurcation along two different axes, creating a characteristic saddle-point domain wall morphology and associated novel dipolar topology, removing the need for screening charge accumulation and associated conductivity enhancement.

1. Introduction

Nonuniform polarization textures in ferroelectrics is a fertile ground for rich novel materials physics. One of the implications of the nonuniform distribution of polarization is the emergence of the bound charges at the polarization discontinuities or, in general, at the points where the divergence of the polarization vector field is nonzero. Bound charges induce the electric field which is energetically costly. Accordingly, the system tends to maintain its internal electric neutrality, however complex the polarization distribution is. Then the neutrality implies that either the polarization vector field should be divergenceless, or that the bound charges should be screened by free carriers of the semiconducting nature. The nonuniform and almost divergenceless polarization textures were mostly found in the multiaxial ferroelectrics[1,2] for which spontaneous polarization vector can rotate.

Y. Tikhonov, V. M. Vinokur, I. Luk'yanchuk
University of Picardie
Laboratory of Condensed Matter Physics
Amiens 80039, France

Y. Tikhonov
Faculty of Physics
Southern Federal University
5 Zorge Street, Rostov-on-Don 344090, Russia

J. R. Maguire, C. J. McCluskey, J. P. V. McConville, A. Kumar, J. M. Gregg
Centre for Nanostructured Media
School of Mathematics and Physics
Queen's University Belfast
Belfast BT7 1NN, UK

H. Lu, A. Gruverman
Department of Physics and Astronomy
University of Nebraska–Lincoln
Lincoln, NE 68588, USA

D. Meier
Department of Materials Science and Engineering
Norwegian University of Science and Technology (NTNU)
Trondheim 7491, Norway

A. Razumnaya
Jožef Stefan Institute
Jamova Cesta 39, Ljubljana 1000, Slovenia

A. Razumnaya, V. M. Vinokur
Terra Quantum AG
Kornhausstrasse 25, St. Gallen CH-9000, Switzerland
E-mail: vv@terraquantum.swiss

V. M. Vinokur
Physics Department
City College of the City University of New York
160 Convent Avenue, New York, NY 10031, USA

ADVANCED
SCIENCE NEWS
www.advancedsciencenews.com

ADVANCED
MATERIALS
www.advmat.de

There, to avoid bound charges formation, the system facilitates divergenceless complex dipolar topological excitations patterns, such flux-closure domains,[3] dipolar vortices,[4,5] skyrmions,[6,7] merons,[8] and Hopfions.[9]

For uniaxial ferroelectrics, where only two opposite polar orientations are possible, it has so far been assumed that the appearance of the head-to-head (H–H) and tail-to-tail (T–T) charged domain walls is unavoidable when antiparallel components of polarization meet. Typically, charged domain walls in uniaxial ferroelectrics demonstrate electrical conduction characteristics that are distinctly different from the domains that they surround. For example, in ErMnO$_3$ and YMnO$_3$, the conduction at T–T walls is significantly enhanced.[10–14] In LiNbO$_3$, the change in conduction is particularly dramatic: When H–H charged domain walls straddle interelectrode gaps, device conductivities have been seen to increase by up to 12 orders of magnitude.[15–18]

Here, we report an alternative mechanism wiping out the polarization discontinuity (appearing when antiparallel domains meet) in the uniaxial ferroelectrics possessing low domain wall conductivity. This mechanism consists in forming the specific configuration of the polarization vector field with the mutual domain bifurcation. It creates the characteristic saddle-point domain wall morphology removing the need for the screening charge accumulation and associated conductivity enhancement. Our work presents the theoretical findings on the domain structure in ferroelectrics with low domain wall conductivity and the experimental results obtained for an exemplary uniaxial ferroelectric, lead germanate Pb$_5$Ge$_3$O$_{11}$ (PGO). Our findings fully complete the general description of the structure of the charged domain walls in uniaxial ferroelectrics, ranging from PGO and TGS, with low domain wall conductivity to ferroelectrics with high domain wall conductivity, like ErMnO$_3$, YMnO$_3$, and LiNbO$_3$.

2. Results and Discussion

The lead germanate, PGO, is a uniaxial ferroelectric that undergoes a second order phase transition at ≈450 K. Upon cooling, a symmetry reduction from hexagonal (space group $P\bar{6}$) to trigonal (P3) leads to emergence of a spontaneous polarization with a room temperature value of the order of ≈5 µCcm^{-2}.[19–21] The loss of the centre of symmetry associated with the phase transition results in only two possible domain variants, with polarization along the [001] and [00$\bar{1}$] directions. Polarization reversal under an applied electric field proceeds via canonical domain nucleation and domain wall motion.[22,23] The characteristically observed room temperature microstructure of PGO is often described as consisting of domains of one type, elongated along the polar axis, within a matrix of the other.[23,24] Elongated domain shapes are expected to help reduce the electrostatic energy of the system, when charged head-to-head (H–H) and tail-to-tail (T–T) domain wall regions seem to be unavoidable. The appearance of the domain pattern is dependent on the viewing direction: Elongated domains are observed on the nonpolar surface (the surface parallel to the polar axis), while more isotropic shapeless domains are visible on the polar face (**Figure 1**a,b). In contrast to ErMnO$_3$, YMnO$_3$, and LiNbO$_3$
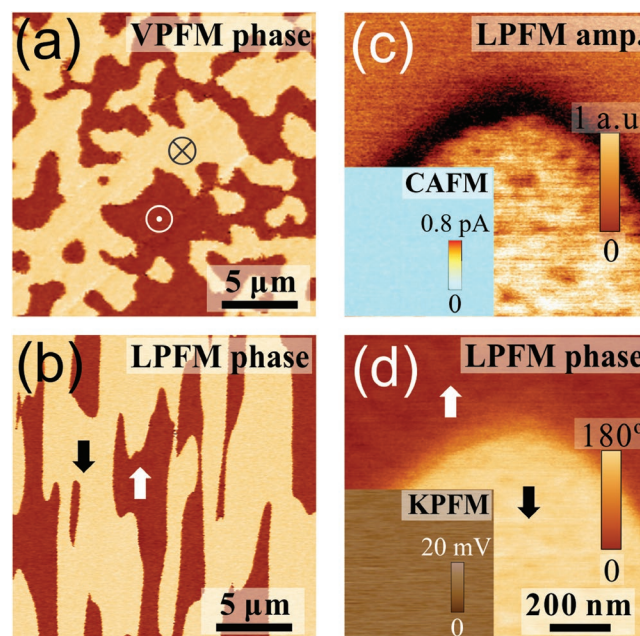

Figure 1. Characteristic features of domain microstructures in lead germanate. a) VPFM phase image of the domain structure on the polar (001) surface. b) LPFM phase image of the domain structure on the nonpolar (010) surface. c,d) High-magnification LPFM amplitude (c) and phase (d) images of the T–T domain wall visualized on the nonpolar (010) surface. Insets in (c) and (d) are the cAFM and KPFM maps, respectively, acquired in the same area showing no conductivity and no surface potential variations at the T–T domain wall.

systems, the investigations of the H–H or T–T domain walls on nonpolar (010) surfaces in PGO by conducting atomic force microscopy (cAFM) and Kelvin probe force microscopy (KPFM)[24] revealed no evidence of the conductivity or surface potential variations expected at these walls (Figure 1c,d).

To better understand the seemingly unique nature of the PGO microstructure, we employed tomographic piezoresponse force microscopy (TPFM).[25] The TPFM involves rastering the tip of a scanning probe microscope while applying a significant compressive force, of several micronewtons, to sequentially remove thin layers from the specimen surface. Imaging can be done either at the same time as the machining (and under the same conditions), or in separate scans taken between machining runs, in which more conventional tip pressures can be applied. We took the latter approach. Machining and subsequent PFM imaging in the same scanned area allow a collection of a series of planar domain images to be acquired at different depths into the sample (**Figure 2**a). Here, the vertical PFM phase maps (where colors indicate the two domain variants present), taken at differing depths below a polished (001) polar surface of single-crystal PGO, are stacked alongside equivalent images in which the domain walls are highlighted. Such images allow 3D rendering of domain structure consisting of antiparallel counter domains (Figure 2b,c).

Several important observations are made. First, the milling processing associated with the TPFM has not had any noticeable effect on the PGO domain structure: The general form and scale of the domains observed on milled (001) surfaces are similar to those initially seen on the unmilled surface, even at
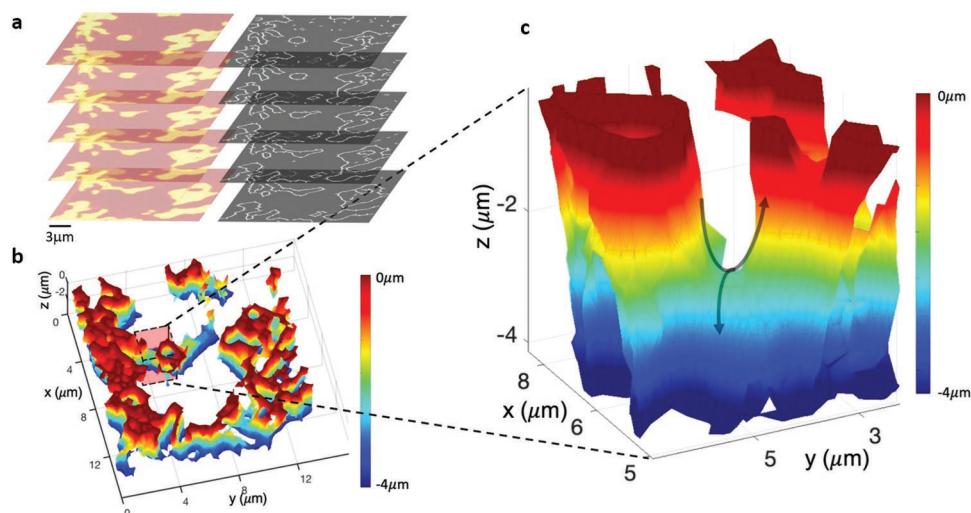
Figure 2. Domain wall saddle points in lead germanate. a) Vertical PFM phase (left) of lead germanate at different depths into the crystal, obtained by PFM tomography, along with the domain wall trace inferred from the PFM (right). The scale bar is 3 μm. b) 3D domain wall reconstruction, obtained by triangulating the points identified as the the DW surface in (a). c) A zoomed in view of the domain wall saddle point highlighted in (b). The arrows show the intersecting maxima and minima, and the color scale represents z height.

depths of several microns (Figure S1a,b, Supporting Information). Moreover, the 3D domain arrangement reconstructed from the TPFM images shows the characteristic elongated domain morphologies on the same scale as those observed on nonpolar surfaces (Figure S1c-l, Supporting Information). Second, the possibility of mechanically induced switching due to the flexoelectric effect[26] can be ruled out as there is no preferential growth of the domains with downward polarization, at the expense of the upward domains, as would be expected from the flexoelectric field pointing away from the pressing tip. Third, the rendered domain wall contains multiple saddle point structures.

The existence and prevalence of saddle points in the domain wall morphology is significant. (More details of the reconstruction of their topological structure are shown in the Figure S2, Supporting Information.) After all, a preconceived microstructural picture of cigar-like ellipsoids of one domain variant embedded in a matrix of the other would not have produced them and would instead have been characterized by ellipsoidal maxima and minima (cup and rounded cone-type features like those typically seen in 3D renders of LiNbO$_3$ domain walls[17,27]). The saddle points instead suggest that when the two domain variants meet (H–H or T–T), they both bifurcate, but in different bifurcation planes (in the experiments, bifurcation planes appear to both be parallel to the [001] and at an angular separation of 120°, commensurate with the crystal trigonal symmetry).

To gain further insight into the internal domain structure of the PGO, we perform the phase-field modeling of the bumping polarization fluxes (see Experimental Section for details). **Figure 3** displays the simulated structure of the interpenetrating domains with the respective up- and down- polarization directions shown by white arrows. The fair correspondence between the experimentally observed (Figure 1) and simulated (Figure 3a) domain textures is clearly seen. To display the spatial polarization distribution, we perform the inner-corner cut

of the simulated PGO sample (see Figure 3a). The structure reveals the self-similar configuration with branching domains. The vertical cross-cuts demonstrate the inclined domain walls; the cuts crossing the meanders produce the famed "cigar-shaped" forms. The horizontal cross-cut exposes the irregular pattern of cross-sections of the domains with the DWs highlighted by green lines. Another important feature is that the upper and bottom near-surface regions host the Landau fractal multidomain structure that forms to compensate surface bound charges.[28,29]

Both experimental data and simulations establish the existence of the bent DWs, where, supposedly, the substantial bound charges destabilizing ferroelectricity would have arisen. At the same time, the electric charge, $\rho = -div \, \mathbf{P}$, appears to be vanishingly small in the vicinity of the DW ridges, where it is supposed to be the maximal (see the charge map of the horizontal cross-section area, magnified at the lower plane of Figure 3b). The bound charge at the bent DWs is indeed much smaller than the charge expected from the z-gradient of the spontaneous polarization, $\rho_z = -\partial_z P_z$, presented at the upper plane of Figure 3b; the up- and down-arrows in the upper plane show the directions of the P_z polarization. The solution of the puzzle is that the charge ρ_z is nearly compensated, that is, effectively screened, by the shown in the middle plane charge $\rho_{xy} = -\partial_x P_x - \partial_y P_y$ induced by the transverse, P_x and P_y polarization components; the in-plane arrows in the middle plane indicate the directions of the transverse polarization. Hence, the total bound charge arising near the bent DWs, $\rho = \rho_z + \rho_{xy}$, comes out much smaller than ρ_z. The more detailed distribution of the polarization fields and charges is presented in Figure S3, Supporting Information. This figure also reveals the softening of the H–H and T–T DWs resulting in their broadening with respect to the vertical uncharged DWs, which occurs due to the interplay between the polarization and electric field induced by the bound charges as predicted in refs. [29, 30].
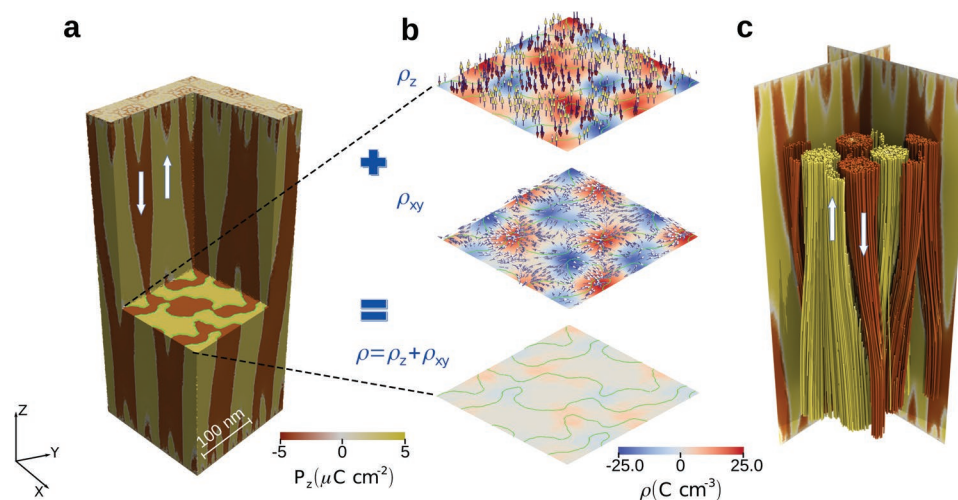
Figure 3. The domain networking structure. a) An inner-corner cut of the rectangular uniaxial PGO sample. The panel displays the simulated structure of interpenetrating polarization domains with the respective up- and down- polarization directions shown by white arrows. The magnitude of the z-component of the polarization, P_z, is quantified by the color legend. The upper and bottom near-surface regions host Landau fractal multidomain structure arising to compensate surface bound charges. The green contours depict the cross sections of the domain walls. b) The charge map of the horizontal cross-section area shown in panel (a). The upper plane displays the spontaneous polarization charge $\rho_z = -\partial_z P_z$, the up- and down-arrows in the upper plane showing the local directions of the P_z polarization. The middle plane displays the charge $\rho_{xy} = -\partial_x P_x - \partial_y P_y$ induced by the transverse polarization whose local directions are shown by the in-plane arrows. The bottom plane displays the total resulting charge $\rho = -div\,\mathbf{P}$ and demonstrates that ρ_{xy} effectively screens ρ_z so that the total charge, ρ, is vanishingly small in the vicinity of the inclined DWs. c) Visualization of the complex network of polarization lines formed by the counter-flowing polarization fluxes corresponding to the "up" and "down" domains.

The obtained smallness of the bound charges at DWs demonstrates the basic concept that uniaxial ferroelectrics maintain the divergenceless character of the polarization because of the specific texture of the polarization vector field. The bound charges are indeed small since they induce the electric field which is energetically costly. Accordingly, the system tends to maintain its internal electric neutrality.

Figure 3c displays the polarization distribution as flux bundles visually identical to the countercurrents in incompressible liquid that slightly deviate from their original paths to avoid the clash. The counterflowing streams in the liquid correspond thus to the oppositely oriented polarization domains which bend to avoid the H–H and T–T collisions. Then, the neutrality is provided by the topological entwining of the encountered polarization line streams, separated by the single path-connected DW extended through the system. The neutrality implies that the polarization vector field is divergenceless, hence similar to the velocity field in incompressible liquids. The overall configuration of the polarization pattern forms in accordance with the fundamentals of topological hydrodynamics,[31] and is identical to that of the velocity field of the incompressible liquid flowing in a restricted volume. The energy cost related to the domain bending is far below the expense of the electrostatic energy associated with the onset of uncompensated bound charges. Accordingly, the polarization forms a network of the counterflowing slightly bent domains alternatively carrying "up" and "down" polarization fluxes. It is the transverse component of the polarization that ensures that the domains with opposite flux avoid the mutual clash.
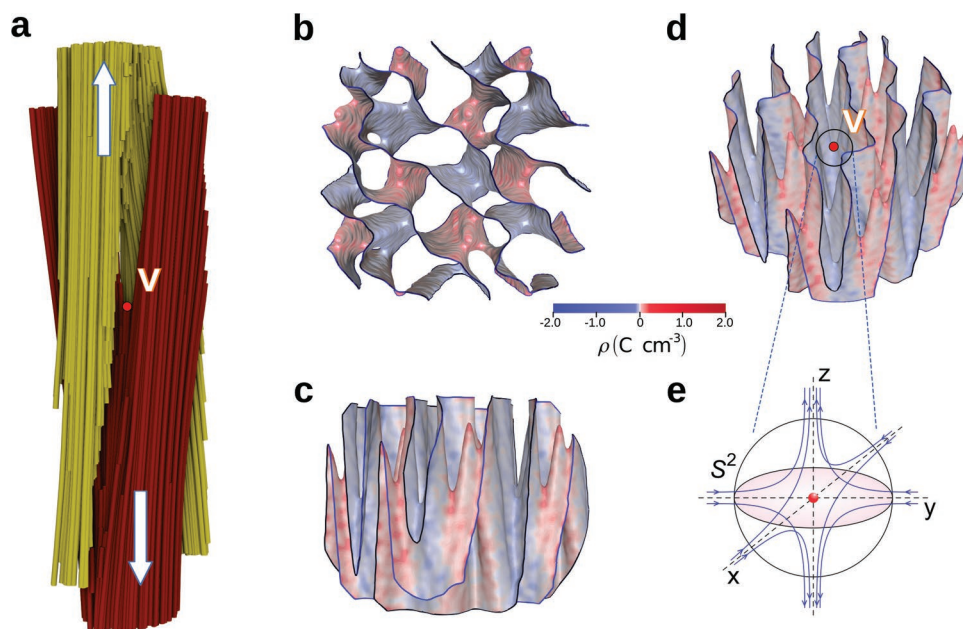
The counterflowing domains are separated by domain walls as shown in detail in **Figure 4**. Figure 4a presents an essential building block of the domain network, the two branching streams that assume the V-shape clash-avoiding scissoring configuration. The global image of the domain wall is shown in Figure 4b and constitutes a path-connected topological manifold. Figure 4c shows the side view of the DWs manifold. Figure 4d is a tilted view clearly exposing the scissoring point $\mathbb{V}$ marked red. This point realizes a saddle node singularity of the polarization vector field $\mathbf{P}$ (Figure 4e). The node is characterized by the singularity index calculated as the sign of the Jacobian of the field $\mathbf{P}$ at point $\mathbb{V}$, $N = \mathrm{sgn}\det\|\partial_i P_j\|$.[32] Accordingly, N is equal to +1 when the outcoming in the $\pm z$-direction polarization fluxes of T–T encountering domains captivate the polarization flow converging to the $\mathbb{V}$-point from the x–y plane; this situation is shown in Figure 4e. In the opposite case of the H–H domains encountering, $N = -1$.

The singularity of the field at point $\mathbb{V}$ is a topological property. To see that, let S^2 be a closed sphere centered at $\mathbb{V}$ that is pierced by the polarization field $\mathbf{P}$. Consider now the map of S^2 onto the space of the tips of the normalized vector $\mathbf{n} = \mathbf{P}\,/\,P$ which is also a 2D sphere S'^2. Thus, each point $\in S^2$ has an image on S'^2 corresponding to the vector $\mathbf{n}$ at this point. This correspondence is characterized by the degree of the map $S^2 \xrightarrow{f} S'^2$,[32]

$$\deg f = \frac{1}{4\pi} \int_{S^2} \left(\mathbf{n} \cdot [\partial_\theta \mathbf{n} \times \partial_\varphi \mathbf{n}] \right) d\theta d\varphi \qquad (1)$$

where the integration is performed over the surface S^2, with φ and θ being the spherical coordinates. This quantity is an integer number giving the number of times that the image of sphere S^2 is wrapped over the sphere S'^2; hence, it is the topological characteristic of the point $\mathbb{V}$ that does not depend on the choice of the wrapping surface. Importantly, the degree of the map $S^2 \xrightarrow{f} S'^2$ for the sphere surrounding the point $\mathbb{V}$ is identical to the singularity index N for this point, $\deg f = N$. This

**ADVANCED
SCIENCE NEWS**

www.advancedsciencenews.com

**ADVANCED
MATERIALS**

www.advmat.de

Figure 4. The domain wall's topological structure. a) The collision and subsequent splitting of the polarization streams in point $\mathbb{V}$ result in the scissoring pattern. b) The top view of the domain wall. c) The side view of the domain wall. d) Isometric projection of the domain wall. Point V corresponds a scissoring of the streams in (a). (b)–(d) demonstrate that domain wall is a single path-connected surface separating the channels carrying the continuous oncoming streams of polarization fluxes piercing the system. The color map visualizes the effective surface charge density, σ, quantified by the the color legend. Importantly, the value of σ is substantially less than the polarization reversal $\Delta P_z \simeq \pm 10 \ \mu C \ cm^{-2}$ at the head-to-head and tail-to-tail domain walls because of the lateral screening effect. e) The enlarged vicinity of the saddle singular point $\mathbb{V}$. The pink disc stands for the piece of the plain tangent to the saddle surface in the point $\mathbb{V}$. The blue lines depict the polarization flow in the vicinity of the singularity.

fundamental statement establishes the deep relation between the topological properties of the point $\mathbb{V}$ and the differential properties of the polarization vector field, **P**, in its vicinity. Therefore, the stability of the domain scissoring structure hosting the singular saddle point $\mathbb{V}$ is topologically protected.

It is clearly seen that in the close vicinity of the saddle point $\mathbb{V}$, the shape of the DW is the saddle surface, that is, a surface that curves up and curves down in perpendicular directions. The color of the manifold (see Figure 4d) represents the effective surface charge density at the manifold which remains indeed low. The DW assumes the configuration that minimizes its energy under constraints imposed by the boundary conditions stemming from the domains' collisions. The shape of the DW is similar to that of the soap film, which is attached to the outer fixed frame and shapes itself to minimize its surface energy.[33] The DW is thus an exemplary realization of a concept widely known in mathematics as the Lagrange minimal surface problem.[34] Note that our multiconnected domain wall presents a more general case than the usual minimal surface of the soap film: it accounts also for the minimization of the non-local energy of bending of the DW-generating counter-flowing polarization field lines.

The above consideration of the domain wall structure in uniaxial ferroelectrics is of universal character since it is based on the fundamental topological principles implemented in a general form of the Ginzburg–Landau functional. The only parameter that drives the topology of the H–H and T–T DWs is the concentration of the free charge carriers that screen the bound charges due to polarization. In the PGO material, we assumed the absence of the screening charges that corroborates

with the absence of conductivity of the DWs. Our simulations (see Experimental Section for details) show that the single-path-multiconnected domain walls and the associated saddle points cease to exist upon increasing the concentration of the screening charges. Figure S4, Supporting Information, demonstrates how these unique topological features emerge at the low concentration of the free screening charges and disappear upon increasing their concentration. The saddle points' disappearance is followed by the simultaneous breaking up of the single-path-connected DW into the set of the multitude of non-connected surfaces. The simulation results shown in Figure S4, Supporting Information, are compared with the experimental data for several uniaxial ferroelectrics (see Figure S5, Supporting Information). Comparison shows that a good number of uniaxial ferroelectrics, including the TGS, ErMnO₃, and LiNbO₃, follow the described-above scenario of evolution of the topology of the DWs upon changing of the charge carrier concentration.

3. Conclusion

Combining experimental and theoretical studies of the domain structure in the lead germanate, we reveal an effect of eliminating the bound charges arising in the H–H and T–T configurations. Polarization bifurcations at the H–H and T–T domain walls along two different axes create characteristic saddle point like domain junctions, associated with the distinct dipolar topology. Eliminating polarization discontinuities by screening results in the vanishing of bound charges and the associated

conductivity at the H–H and T–T domain walls in the PGO. It is expected that the obtained results will prompt high-resolution microscopy studies of the detailed structure of these notionally charged domain walls. The method resulting in the successful description of the polarization texture in the PGO is based on the similarity of the polarization vector field behavior to the flow of an incompressible fluid. This general consideration well applies to other uniaxial ferroelectrics and gives a new dimension to the study of topological textures in polar solids.

4. Experimental Section

Tomographic Piezoresponse Force Microscopy: The TPFM experiments (Figure 2) were performed on the polar face of the same lead germanate crystal, using an Asylum Research MFP-3D Infinity AFM system with an internal lock-in amplifier. The TPFM technique employed involves simultaneous PFM imaging of the domain structure and AFM machining. A conductive diamond-coated silicon probe was scanned over the surface at a speed of 75 μms^{-1}. The probe has a high stiffness constant of 80 Nm^{-1}, which, when combined with a high AFM deflection setpoint, produces a significant force on the sample surface. This resulted in the sequential removal of layers of material at a rate of approximately 0.2 μm per scan, up to a total depth of 4 μm, over a 20 μm $\times$ 20 μm region. Domain information was collected simultaneously via PFM (AC bias amplitude 2 V and frequency 3.0 MHz) allowing for the domain evolution through the depth of the crystal to be mapped. The locations of the domain walls at various depths were extracted by taking the gradient of the PFM phase maps collected during TPFM. Using these domain wall locations, a 3D reconstruction of the domain wall surface (Figure 2a) was created using the "alphaShape" triangulation function, implemented in MATLAB. All PFM data were collected at room temperature under ambient conditions.

Phase-Field Method: The simulations were based on the minimization of the Ginzburg–Landau (GL) functional, $F = \iiint f dV$, with respect to the magnitude of the z-directed spontaneous polarization, P, playing the role of the order parameter in the uniaxial ferroelectric material, and with respect to the electric potential, φ, determining the electric field $E = -\nabla \varphi$ and elastic strains u_{ij}.

The free energy density is

$$f = \frac{A}{2}(T - T_c)P^2 + \frac{b^{(u)}}{4}P^4 + \frac{c}{6}P^6 + \frac{G}{2}(\nabla P)^2 \qquad (2)$$
$$+ P\partial_z\varphi - \frac{1}{2}\varepsilon_0\varepsilon_b\left[(\nabla\varphi)^2 + \delta^{-2}\varphi^2\right] - C_{ijkl}Q_{kl33}u_{ij}P^2 + \frac{1}{2}C_{ijkl}u_{ij}u_{kl}$$

Here, the repetitive indices imply the summation over these indices. The total polarization including also a non-critical part induced by the depolarization field is given by $P = Pz + \varepsilon_0\varepsilon_i E$, where it is assumed that the background dielectric constant ε_b is isotropic.

The relevant for the uniaxial case electrostrictive constants, Q_{1133}, $Q_{2233} = 0.14$, $Q_{3333} = 0.20$ [10^8 cm^4 C^{-2}] and stiffness coefficients, C_{1111}, $C_{2222} = 6.84$, C_{1133}, $C_{2233} = 1.79$, $C_{3333} = 9.48$ [10^{10} m^{-2} N], were taken from refs. [19] and [35], respectively. The numerical values of the GL coefficients were obtained from fitting the experimental data reported in the preceding studies of the PGO[19] (see Figure S6, Supporting Information), $A = 1.09 \times 10^7$ C^{-2} m^2 N K^{-1}, $c = 3.3 \times 10^{14}$ C^{-6} m^{10} N, $G = 8.26 \times 10^{-10}$ C^{-2} m^4 N, the vacuum dielectric permittivity $\varepsilon_0 = 8.85 \times 10^{-12}$ C^2 m^{-2} N^{-1}, and the background non-critical part of the dielectric constant $\varepsilon_b = 20$). The zero-strain fourth order coefficient $b^{(u)}$ required for strain-dependent functional, Equation (2), was calculated using the zero-stress coefficient $b^{(\sigma)} \approx 0$, obtained from fitting the experimental data, using the renormalization procedure described in ref. [36] ($b^{(u)}/4 = b^{(\sigma)}/4 + (C_{1111} + C_{1122})Q_{1133}^2 + \frac{1}{2}C_{3333}Q_{3333}^2 + 2C_{1133}Q_{1133}Q_{3333} \approx 4.75 \times 10^9$ C^{-4} m^6 N).

Incorporation of the screening free carriers into the model was accomplished via the screening length $\delta \approx (a_0/4n^{1/3})^{1/2}$,[37] where

$a_0 = 0.053$ nm was the Bohr radius. The typical value of δ, reproducing the path-connected DW containing saddle points and having polarization bifurcations, was selected above 7 nm corresponding to the carrier concentration below 2×10^{10} cm^{-3}. For smaller δ, the structure transforms into the series of the head-to-head or tail-to-tail domains separated by 2D domain wall membrane comprising hills and potholes. The corrugation has the tendency to become more smooth with a further decrease of δ. Below $\delta \approx 5$ nm (corresponding to $n \approx 1.5 \times 10^{11}$ cm^{-3}), the H–H (T–T) DW becomes practically flat (see Figure S4, Supporting Information).

To perform numerical calculations, the phase-field method implemented via the FEniCS software package was used.[38] Nonlinear system of partial differential equations to solve comes from the variation of the free-energy functional, Equation (2), with respect to polarization P:

$$-\gamma\frac{\partial P}{\partial t} = \frac{\delta F}{\delta P} \qquad (3)$$

where γ is the time-scale parameter, whose value is irrelevant for our current case and is taken to be equal unity.

The nonlinear system of Equation (3) is closed by the linear system corresponding to electrostatic (with screening) and elastic equations:

$$\varepsilon_0\varepsilon_b[\nabla^2 - \delta^{-2}]\varphi = \partial_z P \qquad (4)$$

$$C_{ijkl}\partial_j(u_{kl} - Q_{kl33}P^2) = 0 \qquad (5)$$

The computational domain was a rectangular box with dimensions $200 \times 200 \times 500$ nm that was partitioned into tetrahedrons with the help of 3D mesh generator gmsh.[39] The encountering of oncoming antiparallel domains was achieved by the special choice of boundary conditions for polarization at the top and at the bottom of the sample. At the top and bottom surfaces of the computational domain, the Dirichlet boundary conditions were imposed, $P_{top} = P'\sin(2\pi x/100 + \pi)$ $\sin(2\pi y/100)$, $P_{bottom} = P'\sin(2\pi x/100)\sin(2\pi y/100)$, where $P' = 5$ μC cm^{-2} was the value close to the equilibrium value of polarization throughout the volume of the sample. The phase shift between polarization distributions at the top and bottom rectangular surfaces was properly selected to ensure encountering of the oppositely polarized domains in the bulk of the sample. In the x and y directions, the boundary conditions on P and φ were set to be periodic.

Approximation of time derivative at the left-hand side of the variation (3) was accomplished by the BDF2 stepper with the variable time step.[40] At the first time step of the simulation, the values of the polarization in the computational domain were taken randomly from the [-10^{-4}, 10^{-4}] μC cm^{-2} interval. The solution of the nonlinear system of equations was accomplished by the Newton-based nonlinear solver with the line search and generalized minimal residual method with the restart.[41,42] The linear system resulting from the discretization of Equations (4) and (5) was solved using the generalized minimal residual method with the restart.

Supporting Information

Supporting Information is available from the Wiley Online Library or from the author.

Acknowledgements

**ADVANCED
SCIENCE NEWS**

www.advancedsciencenews.com

**ADVANCED
MATERIALS**

www.advmat.de

[1] M. E. Lines, A. M. Glass, *Principles and Applications of Ferroelectrics and Related Materials*, Oxford University Press, Oxford, UK **2001**.

[2] A. K. Tagantsev, L. E. Cross, J. Fousek, *Domains in Ferroic Crystals and Thin Films*, Springer, New York **2010**.

[3] R. McQuaid, L. McGilly, P. Sharma, A. Gruverman, J. Gregg, *Nat. Commun.* **2011**, *2*, 404.

[4] L. Lahoche, I. Luk'yanchuk, G. Pascoli, *Integrated Ferroelectrics* **2008**, *99*, 60.

[5] A. Yadav, C. Nelson, S. Hsu, Z. Hong, J. Clarkson, C. Schlepütz, A. Damodaran, P. Shafer, E. Arenholz, L. Dedon, D. Chen, A. Vishwanath, A. M. Minor, L. Q. Chen, J. F. Scott, L. W. Martin, R. Ramesh, *Nature* **2016**, *530*, 198.

[6] Y. Nahas, S. Prokhorenko, L. Louis, Z. Gui, I. Kornev, L. Bellaiche, *Nat. Commun.* **2015**, *6*, 8542.

[7] S. Das, Y. Tang, Z. Hong, M. Gonçalves, M. McCarter, C. Klewe, K. Nguyen, F. Gómez-Ortiz, P. Shafer, E. Arenholz, V. A. Stoica, S.-L. Hsu, B. Wang, C. Ophus, J. F. Liu, C. T. Nelson, B. Prasad, A. B. Mei, D. G. Schlom, J. Íñiguez, P. García-Fernández, D. A. Muller, L. Q. Chen, J. Junquera, L. W. Martin, R. Ramesh, *Nature* **2019**, *568*, 368.

[8] Y. Wang, Y. Feng, Y. Zhu, Y. Tang, L. Yang, M. Zou, W. Geng, M. Han, X. Guo, B. Wu, X. L. Ma, *Nat. Mater.* **2020**, *19*, 881.

[9] I. Luk'yanchuk, Y. Tikhonov, A. Razumnaya, V. Vinokur, *Nat. Commun.* **2020**, *11*, 2433.

[10] D. Meier, J. Seidel, A. Cano, K. Delaney, Y. Kumagai, M. Mostovoy, N. A. Spaldin, R. Ramesh, M. Fiebig, *Nat. Mater.* **2012**, *11*, 284.

[11] J. Mundy, J. Schaab, Y. Kumagai, A. Cano, M. Stengel, I. P. Krug, D. M. Gottlob, H. Doganay, M. E. Holtz, R. Held, Z. Yan, E. Bourret, C. M. Schneider, D. G. Schlom, D. A. Muller, R. Ramesh, N. A. Spaldin, D. Meier, *Nat. Mater.* **2017**, *16*, 622.

[12] D. R. Småbråten, Q. N. Meier, S. H. Skjærvø, K. Inzani, D. Meier, S. M. Selbach, *Phys. Rev. Mater.* **2018**, *2*, 114405.

[13] M. Cambell, J. McConville, R. McQuaid, D. Prabhakaran, A. Kumar, J. M. Gregg, *Nat. Commun.* **2016**, *7*, 13764.

[14] P. W. Turner, J. P. V. McConville, S. J. McCartan, M. H. Campbell, J. Schaab, R. G. P. McQuaid, A. Kumar, Marty Gregg, *Nano Lett.* **2018**, *18*, 6381.

[15] C. Godau, T. Kämpfe, A. Thiessen, L. M. Eng, A. Haußmann, *ACS Nano* **2017**, *11*, 4816.

[16] C. Werner, S. Herr, K. Buse, B. Sturman, E. Soergel, C. Razzaghi, I. Breunig, *Sci. Rep.* **2017**, *7*, 9862.

[17] H. Lu, Y. Tan, J. P. McConville, Z. Ahmadi, B. Wang, M. Conroy, K. Moore, U. Bangert, J. E. Shield, L.-Q. Chen, J. M. Gregg, A. Gruverman, *Adv. Mater.* **2019**, *31*, 1902890.

[18] J. P. V. McConville, H. Lu, B. Wang, Y. Tan, C. Cochard, M. Conroy, K. Moore, A. Harvey, U. Bangert, L. Q. Chen, A. Gruverman, J. M. Gregg, *Adv. Funct. Mater.* **2020**, *30*, 2000109.

[19] H. Iwasaki, S. Miyazawa, H. Koizumi, K. Sugii, N. Niizeki, *J. Appl. Phys.* **1972**, *43*, 4907.

[20] S. Nanamatsu, H. Sugiyama, K. Doi, Y. Kondo, *J. Phys. Soc. Jpn.* **1971**, *31*, 616.

[21] H. Iwasaki, K. Sugii, T. Yamada, N. Niizeki, *Appl. Phys. Lett.* **1971**, *18*, 444.

[22] A. Gruverman, N. Y. Ponomarev, K. Takahashi, *Jpn. J. Appl. Phys.* **1994**, *33*, 5536.

[23] V. Y. Shur, A. Gruverman, V. V. Letuchev, E. Rumyantsev, A. Subbotin, *Ferroelectrics* **1989**, *98*, 29.

[24] O. Bak, T. S. Holstad, Y. Tan, H. Lu, D. M. Evans, K. A. Hunnestad, B. Wang, J. P. McConville, P. Becker, L. Bohatý, I. Lukyanchuk, V. M. Vinokur, A. T. J. van Helvoort, J. M. Gregg, L.-Q. Chen, D. Meier, A. Gruverman, *Adv. Funct. Mater.* **2020**, *30*, 2000284.

[25] J. J. Steffes, R. A. Ristau, R. Ramesh, B. D. Huey, *Proc. Natl. Acad. Sci. USA* **2019**, *116*, 2413.

[26] H. Lu, C.-W. Bark, D. E. de los Ojos, J. Alcala, C. B. Eom, G. Catalan, A. Gruverman, *Science* **2012**, *336*, 59.

[27] B. Kirbus, C. Godau, L. Wehmeier, H. Beccard, E. Beyreuther, A. Haußmann, L. M. Eng, *ACS Appl. Nano Mater.* **2019**, *2*, 5787.

[28] B. A. Strukov, A. P. Levanyuk, *Ferroelectric Phenomena in Crystals: Physical Foundations*, Springer, Berlin, Germany **2012**.

[29] F. De Guerville, I. Luk'yanchuk, L. Lahoche, M. El Marssi, *Mater. Sci. Eng., B* **2005**, *120*, 16.

[30] I. A. Luk'yanchuk, L. Lahoche, A. Sené, *Phys. Rev. Lett.* **2009**, *102*, 147601.

[31] V. I. Arnold, B. A. Khesin, *Topological Methods in Hydrodynamics*, Springer, New York **2008**.

[32] B. A. Dubrovin, A. T. Fomenko, S. P. Novikov, *Modern Geometry–Methods and Applications: Part II: The Geometry and Topology of Manifolds*, Springer, New York **2012**.

[33] F. Maggi, A. Scardicchio, S. Stuvard, *arXiv:1807.05200*, **2018**.

[34] U. Dierkes, S. Hildebrandt, F. Sauvigny, in *Minimal Surfaces*, Springer, Berlin, Germany **2010**, pp . 53–90.

[35] N. S. Landolt-Börnstein, *Ferroelectrics and Related Substances: Oxides, Group III*, Vol. *16a*, Springer, Berlin, Germany **1982**.

[36] A. F. Devonshire, *Lond. Edinb. Dublin Philos. Mag. J. Sci.* **1949**, *40*, 1040.

[37] C. Kittel, *Introduction to Solid State Physics*, Wiley, New York **2004**.

[38] A. Logg, K.-A. Mardal, G. N. Wells, *Automated Solution of Differential Equations by the Finite Element Method*, Springer, Berlin, Germany **2012**.

[39] C. Geuzaine, J.-F. Remacle, *Int. J. Numer. Methods Eng.* **2009**, *79*, 1039.

[40] A. Janelli, R. Fazio, *J. Comput. Appl. Math.* **2006**, *191*, 246.

[41] S. Balay, S. Abhyankar, M. F. Adams, J. Brown, P. Brune, K. Buschelman, L. Dalcin, A. Dener, V. Eijkhout, W. D. Gropp, D. Karpeyev, D. Kaushik, M. G. Knepley, D. A. May, L. C. McInnes, R. T. Mills, T. Munson, K. Rupp, P. Sanan, B. F. Smith, S. Zampini, H. Zhang, H. Zhang, PETSc Web page, https://www.mcs.anl.gov/petsc, (accesssed: March 2022).

[42] S. Balay, S. Abhyankar, M. F. Adams, J. Brown, P. Brune, K. Buschelman, L. Dalcin, A. Dener, V. Eijkhout, W. D. Gropp, D. Karpeyev, D. Kaushik, M. G. Knepley, D. A. May, L. C. McInnes, R. T. Mills, T. Munson, K. Rupp, P. Sanan, B. F. Smith, S. Zampini, H. Zhang, H. Zhang, PETSc users manual, Technical Report ANL-95/11 - Revision 3.15, Argonne National Laboratory, https://www.mcs.anl.gov/petsc, (accessed: March 2022).